J. Fluid Mech. (2024), *vol*. 997, A6, doi:10.1017/jfm.2024.757

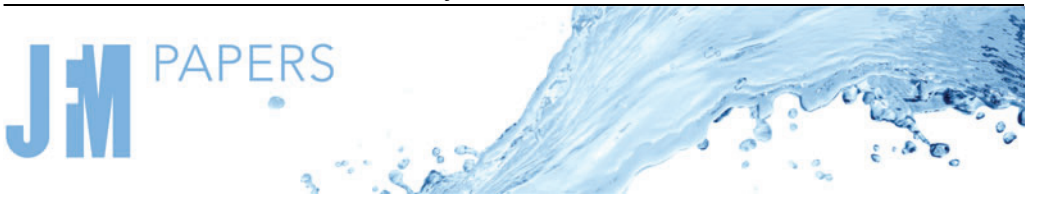

Limiting regimes of turbulent horizontal convection. Part 2. Large Prandtl numbers

Pierre-Yves Passaggia[1,2], **Nadia F. Cohen**[3] **and Alberto Scotti**[2,4,†]

[1]University of Orléans, INSA-CVL, PRISME, EA 4229, 45072 Orléans, France

[2]Department of Marine Sciences, The University of North Carolina at Chapel Hill, NC 27514, USA

[3]Civil and Construction Engineering, OSU, Corvallis, OR 97331, USA

[4]School for Engineering of Matter, Transport and Energy, Arizona State University, AZ 85287, USA

(Received 12 December 2023; revised 18 June 2024; accepted 28 July 2024)

Horizontal convection at large Rayleigh and Prandtl numbers is studied experimentally in a regime up to seven orders of magnitude larger in terms of Rayleigh numbers than previously achieved. To reach Rayleigh numbers up to 10^{17}, the horizontal density gradient is generated using differential solutal convection by a differential input of salt and fresh water controlled by diffusion in a novel experiment in which the zero-net mass flux of water is ensured through permeable membranes. This set-up allows us to accurately measure the Nusselt number in solutal convection by carefully controlling the amount of salt water exchanged through the membranes. Combined measurements of density and velocity across more than five orders of magnitude in Rayleigh numbers show that the flow transitions from the Beardsley & Festa (*J. Phys. Oceanogr.*, vol. 2, issue 4, 1972, pp. 444–455), Shishkina & Wagner (*Phys. Rev. Lett.*, vol. 116, issue 2, 2016, 024302) regime to the Chiu-Webster *et al.* (*J. Fluid Mech.*, vol. 611, 2008, pp. 395–426) regime and frames the present results within the scope of Shishkina *et al.* (*Geophys. Res. Lett.*, vol. 43, issue 3, 2016, pp. 1219–1225), and the theory of Part 1 (Passaggia & Scotti, vol. 997, 2024, *J. Fluid Mech.*, A5). In particular, we show that, even for large Prandtl numbers, the circulation eventually clusters underneath the forcing horizontal boundary, leaving a stratified core without motion. Finally, the previous regime diagrams (Hughes & Griffiths, *Annu. Rev. Fluid Mech.*, vol. 40, 2008, pp. 185–208; Shishkina *et al.*, *Geophys. Res. Lett.*, vol. 43, issue 3, 2016, pp. 1219–1225) are extended by combining the present results at high Prandtl numbers, the results at low Prandtl numbers of Part 1, together with previous results from the literature. This work sets a new picture of the transition landscape of

† Email address for correspondence: adscotti@asu.edu

horizontal convection over six orders of magnitude in Prandtl number and sixteen orders of magnitude in Rayleigh number.

Key words: convection

1. Introduction

Experimental work on horizontal convection (HC) has attracted little attention compared with Rayleigh–Bénard convection. Despite the analysis of Jeffreys (1925), who showed from fundamental thermodynamics that a differential buoyancy gradient along a constant geopotential height requires a residual circulation, the conclusion of Sandström (1908), that only a very shallow surface circulation detached from a stratified interior at rest exists at high Rayleigh number, dominated the thinking on the subject for a long time (Sverdrup, Johnson & Fleming 1942; Defant 1961). This position was later challenged by Rossby (1965) based on laboratory experiments. Rossby showed that HC may indeed lead to a non-negligible overturning flow with a scaling analysis, which provided the first insights that, despite the small convective intensity of HC when compared with the Rayleigh–Bénard problem, HC could still produce a substantial residual circulation and be relevant for real-world applications.

A key difficulty in designing laboratory experiments in HC using heat as a stratifying agent is the need to prevent buoyancy gain or losses along surfaces other than the horizontal surface where forcing is applied. Wang & Huang (2005) used a nearly complete vacuum in a rectangular container to ensure an insulating boundary, while large Styrofoam slabs were used in the experiment of Mullarney, Griffiths & Hughes (2004). Both sets of authors identified a regime transition at $Ra \approx 10^{10}$ for differential heating in water. Each experiment provided similar scaling laws. However, an important difference could be found between the two experiments: the plume observed in the experiment of Wang & Huang (2005) did not fully reach the bottom, whereas the other experiment showed the contrary. Although this may be attributed to the insulating boundary, Gayen, Griffiths & Hughes (2014) performed direct numerical simulations of the set-up of Mullarney *et al.* and recovered a flow very similar to what was observed in the experiment. Therefore, these experiments raised the question of the role of the aspect ratio of the cavity in the flow. Working with differential heating is very attractive at first, as the viscosity of water can be increased (hence the Prandtl number) by using, for instance, glycerol. However, this method simultaneously decreases the Rayleigh number as in Rossby's original experiments, which prevented these experiments from reaching high Rayleigh numbers.

The large-Prandtl- and large-Rayleigh-number regimes have several important applications, ranging from mantle convection to industrial applications such as glass furnaces (Gramberg, Howell & Ockendon 2007; Chiu-Webster, Hinch & Lister 2008). Such regimes were theorized by Gramberg *et al.* (2007), who assumed that the return flow is distributed over the depth of the shallow layer, which makes the thin light layer move with a uniform velocity to the leading order. However, these findings were later questioned by Chiu-Webster *et al.* (2008), who showed that a laminar regime exists where only the densest fluid in the stratified boundary layer penetrates the entire depth of the box, the remainder returning at a shallow depth in a horizontal intrusion immediately adjacent to the boundary layer. In this case, diffusion between the interior and the relatively weak full-depth plume is crucial for both removing the density anomaly in the plume fluid and

maintaining a stratification in the box interior. More recently, Ramme & Hansen (2019) investigated a similar regime but for higher Rayleigh numbers using two-dimensional numerical simulations. They report a transition to a steeper scaling than previously reported in Chiu-Webster *et al.* (2008). They report that the distribution of the forcing has only a small impact on the dynamics and, similarly, on the effect of shear-free or no-slip boundary conditions. They also noticed that the onset of instability introduces a steeper scaling for the Nusselt and Péclet numbers at Rayleigh numbers between 10^8 and 10^9, which they conjectured to be associated with the transition observed in Shishkina & Wagner (2016). However, it should be recalled that the transition observed in Shishkina & Wagner (2016) was not induced by the onset of instabilities. It should also be noted that local steeper scaling than Rossby's 1/5, as, for instance, reported by Gayen *et al.* (2014), is associated with stability transitions. In addition, the effect of the aspect ratio remains to be examined at large Prandtl numbers, since in the Shishkina & Wagner (2016) theory, the circulation has to span the entire depth of the domain, hence requiring, for instance, domains with large aspect ratios.

Griffiths & Gayen (2015) considered the problem of HC forced by spatially periodic forcing. Their results showed that, for high Rayleigh numbers and small aspect ratios, the core would indeed fill with dense fluid and maintain a stratified interior. Their forcing, localized on a length scale smaller than the depth of the domain, and with variation in both horizontal directions, shows turbulence throughout the domain. Associated experiments were performed by Rosevear, Gayen & Griffiths (2017), where they observed that the Nusselt number (a non-dimensional measure of the buoyancy flux) had a steeper scaling with respect to the Rayleigh number than the (laminar) Rossby scaling or the entrainment regime (Hughes & Griffiths 2008) and the intrusion regime (Chiu-Webster *et al.* 2008). Here, we revisit their experiments, replacing porous brass plates with permeable membranes (Krishnamurti 2003), which allows accurate measurements of the Nusselt number, as previously suggested in the experiment of Mullarney *et al.* (2004). We further improve the method by providing evidence that steady states are reached for each experiment.

More recently, Matusik & Llewellyn-Smith (2019) analysed the response of surface buoyancy flux-driven convection to localized mechanical forcing where salt- and fresh-water fluxes were directed directly into the tank with pumps, while excess water was allowed to exit as an overflow. This set-up has the advantage of driving a localized surface forcing but cannot be considered as a closed system solely driven by buoyancy. The Whitehead & Wang (2008) and Stewart, Hughes & Griffiths (2012) experiments are also worth mentioning in this context. They used mechanical stirring in the interior of the tank to analyse the relationship between mixing in the interior and its effect on circulation.

However, to this date, neither experiments nor numerical simulations have yet been performed in the large-Rayleigh-number and large-Prandtl-number regime for natural HC. Thus, it is not clear whether the circulation transitions to an intrusion-type regime or whether other transitions may be explored as the Rayleigh number increases towards real-world applications. A flow exhibiting shallow circulation close to the differential buoyancy forcing is known as the intrusion regime, and we take advantage of the results of Chiu-Webster *et al.* (2008) to analyse the present experimental results.

Although it is customary to refer to the ratio of viscosity to diffusivity of a solute as the Schmidt number, for consistency with most of the HC literature, here, we call such a ratio the Prandtl number. For the same reason, we will use the word thermal boundary layer when referring to the concentration boundary layer. To achieve high-Prandtl- and high-Rayleigh-number flows, we use a combination of long tanks with large aspect ratios

and a weakly diffusive stratifying agent. Diffusion of salt ions is a simple and effective alternative to heat to modify the buoyancy of a fluid. Moreover, solid boundaries naturally act as no-flux boundaries. To impose the boundary condition at the surface, we use large sheets of semi-permeable membranes stretched over rectangular tanks of different sizes, which could allow for reaching Rayleigh numbers up to nearly 10^{17}. Using this set-up, our aim is to complete the map initiated in Part 1 (Passaggia & Scotti 2024) and extend the HC regime diagram to large values of the Prandtl number.

In this study, we report experimental results on how the Nusselt number (Nu), the thickness of the boundary layers (λ), the streamfunction (Ψ) and approximate values of the Reynolds number in the centre of the domain depend on the Rayleigh number (Ra), the flux Rayleigh number (Ra_f) and the Prandtl number (Pr) in HC at high Pr for values characteristic of solutal convection in salt where $Pr \approx 610$ (Harned 1954). The results agree with the scaling power laws derived by Shishkina, Grossmann & Lohse (2016) based on the Grossmann & Lohse (2000) framework (GL), the review by Hughes & Griffiths (2008), previous experiments (Miller 1968; Mullarney *et al.* 2004) and previous numerical simulations (Beardsley & Festa 1972; Rossby 1998; Ilicak & Vallis 2012). Our experiments cover the laminar regime I_u^+ (see Shishkina *et al.* 2017; Ramme & Hansen 2019; Reiter & Shishkina 2020), and the high-Pr–high-Ra laminar regime I_u (see Chiu-Webster *et al.* 2008). The results are discussed and mapped within a landscape that includes, to the best of our knowledge, all simulations and experiments performed to this date. We show that the (Ra, Pr) landscape first proposed in the review of Hughes & Griffiths (2008) fits within the theoretical prediction of Shishkina *et al.* (2016) and blends all known HC regimes.

The remainder of the article is organized as follows: the flow set-up and experimental apparatus are presented in § 2; the theoretical scaling laws for large-Prandtl-number HC are then presented in § 3 and tested against the experimental results in § 4; § 5 discusses the phase diagram, including the results of Part 1 at intermediate and low Prandtl numbers, while conclusions are drawn in § 6.

2. Problem description

We consider here the problem of convection in the Boussinesq limit, where the density difference $\Delta\rho = \rho_{max} - \rho_{min}$ across the horizontal surface is assumed to be a small deviation from the reference density ρ_{min} taken as the fresh-water density at room temperature. We use a Cartesian coordinate system where the velocity vector is $\boldsymbol{u} = (u, v, w)^{\mathrm{T}}$, $b = -g(\rho - \rho_{min})/\rho_{min}$ is the buoyancy and g is the acceleration due to gravity along the vertical unit vector $\boldsymbol{e}_z$. The control parameters are the Prandtl and Rayleigh numbers given by

$$Pr = \frac{\nu}{\kappa} \quad \text{and} \quad Ra = \frac{\Delta L^3}{\nu\kappa}, \tag{2.1a,b}$$

where ν and κ are the viscosity and salt diffusivity respectively, L is the horizontal length scale of the domain and $\Delta = -g(\rho_{max} - \rho_{min})/\rho_{min}$. Four geometrically similar tanks, with lengths $L = 0.5$, 1.21, 2 and 4.87 m are used in the experiments. Each tank is a parallelepiped with aspect ratio $\Gamma = L/H = 16.6$ with dimensions $[L, W, H]/L = [1, 1/20, 1/16.66]$, where W is the width of the tank. The buoyancy is imposed on the top surface $z = H$, where H is the height of the tank (figure 1).

The magnitude of the large-scale flow Ψ_{max} is characterized by the maximum of the streamfunction. The latter is defined in terms of the horizontal velocity profile $u(z)$ as $\Psi = \partial u/\partial z$. At the same location, we define λ_u, the thickness of the circulation, and λ_b, the thickness of the stratification. The former is measured by the

location of the maximum in the streamfunction, while the latter is defined by solving $(\rho(\lambda_b) - \rho(\lambda_b)_{min})/(\rho(\lambda_b)_{max} - \rho(\lambda_b)_{min}) = 1/2$. Velocity and buoyancy profiles are measured in the middle of the tank. The flux-Rayleigh number Ra_f is defined in terms of the volume flow rate $\dot{Q}(\rho_{well} - \rho_{tank})/\rho_{tank}$ of salt that is added, at steady state, to the tank

$$Ra_f = \frac{\dot{Q}g(\rho_{well} - \rho_{tank})/\rho_{tank}L^2}{\nu\kappa^2}\left(\frac{L}{W}\right), \tag{2.2}$$

where $g = 9.81\ \mathrm{m\ s^{-2}}$ is the acceleration due to gravity, $\dot{Q}$ is the volume flow rate of fluid input into the system while the subscripts $_{tank}$ and $_{well}$ define where the measurements of density were acquired (see the following section). The latter can be used to obtain the Nusselt number by computing the ratio

$$Nu = Ra_f/Ra, \tag{2.3}$$

which is the convective buoyancy flux normalized with the conductive buoyancy flux imposed at the boundary. Note that a very similar technique was employed in previous experiments to compute the Nusselt number in the case where a flux is imposed through the boundary (Mullarney *et al.* 2004; Griffiths, Hughes & Gayen 2013; Rosevear *et al.* 2017).

The tanks were kept at a constant temperature and covered to prevent convection induced by the building's ventilation. On top of the free surface, Spectrum Labs^{TM}Spectra/Por 5 Reinforced 12–14 kD, 0.280 m wide and up to 15 m long permeable membranes were stretched and kept from sagging into the tank, forming two separate shallow wells, one filled with fresh water, the other with salty water. Each well was continuously stirred using a gear pump to keep the densities uniform in the wells. Each well was supplied with fresh and salt water, respectively, at a constant flow rate of $\dot{Q} = [10, 40, 80, 160]$ ml min^{-1} using a 600 rpm Cole-Parmer^{TM}7523-80 Digital Peristaltic Pump. Note that new tubing was used for each experiment. The wells were fed from two 200 litre tanks, whose capacity was selected so that they could supply even the longest-running experiments (which lasted two months) without interruption. Density measurements were recorded using an Anton Paar^{TM}DM35 densitometer whose calibration was verified to the fourth digit. Each experiment was illuminated using a laser from left to right for the two smaller tanks. In the case of the larger tanks, a laser light sheet was introduced between the two wells and illuminated the tank midsection. At the same location, conductivity measurements were performed using a Conduino (Carminati & Luzzatto-Fegiz 2017) probe to obtain high-resolution profiles of conductivity and, therefore, density. The Conduino probe was calibrated using the Anton® Paar DM35 densitometer. The temperature variation was also checked to be less than 0.3 °C between the top and bottom of the tanks, resulting in a relative buoyancy difference no higher than 6 % of the buoyancy difference due to salinity. Density measurements were performed before and after seeding the flow with the particles used for particle image velocimetry, with a resolution below the millimetre scale for all experiments except for the larger tank which were acquired every centimetre.

Planar two-dimensional particle image velocimetry (PIV) data were recorded using a Nikon D4®. We used a continuous green laser pointer at 532 nm whose beam was expanded through a double concave lens. The camera was equipped with a Nikon® AF-S VR Micro-Nikkor 105 mm f/2.8G IF-ED lenses and the analysis of the experimental data was performed using the Matlab®-based PIV software DPIVSoft (Meunier & Leweke 2003; Passaggia, Leweke & Ehrenstein 2012) to process the images. The resolution of the PIV was 0.0001 cm px^{-1} in the worst case, allowing full resolution of the PIV particles.

The time between two consecutive pictures varied between 1 and 3 s. The top layer was seeded using Cospheric® neutrally buoyant for $\rho = [1.000, 1.02, 1, 13]$ g cc^{-1} monodisperse polyethylene PIV particles with diameters in the range $[40, 50]$ μm that were wetted beforehand with the top layer fluid, mixed in a separate tank, slowly reinjected into the free surface between the wells and left to slowly settle across the layers for a couple of hours until they reached their neutral buoyancy position. The PIV measurements lasted for 45 min, to gather nearly 1000 fields, which corresponds to one turnover time τ_F (see table 1). Subsequent analysis shows that this time scale is sufficient to return to a steady state after disturbing the flow.

For visualization purposes, figure 2 shows the development of the circulation in a tank with the same set-up used in the experiments described here, but with a smaller aspect ratio ($\Gamma = 4$). Dye was released on the right part of the tank, near the stable layer, and propagated within the turbulent plume, eventually filling the tank with heavier fluid. Although this series of images is reminiscent of the dynamics shown in previous experiments using heat (Mullarney *et al.* 2004), the steady state reached in the case of salt is rather different, and the remainder of the manuscript links theoretical arguments to direct observations and measurements of density and velocity profiles to determine the nature of steady-state HC flow at large Rayleigh and large Prandtl numbers.

3. Scaling and regimes of HC at large Prandtl numbers

We begin by reviewing the existing scaling laws derived in the limit of large Prandtl numbers and report the exponents for heat and momentum exchanges in HC. It is interesting to note that, for large Prandtl numbers, the regime diagram in the (Ra, Pr) plane, as theorized by Hughes & Griffiths (2008), does not agree with the regime diagram suggested by Shishkina *et al.* (2016). In the next subsection, we review these regimes and point out the subtle differences that characterize each of them. Central to the discussion is the Paparella & Young (2002) inequality, which relates the mean mechanical dissipation of the system with the buoyancy sink through the horizontal boundary to discuss the role of the aspect ratio of the domain at large Prandtl numbers.

3.1. *Rossby's (1965) laminar regime I_l revisited (Shishkina & Wagner 2016)*

Rossby's laminar regime follows from the steady buoyancy boundary-layer equation, which is obtained from the Navier–Stokes equations in the Boussinesq limit and allows for writing an advection–diffusion balance in the boundary layer (see Part 1 for a thorough derivation)

$$ub_x + wb_z = \kappa b_{zz}. \tag{3.1}$$

The dominant terms in this expression reduce to $U\Delta/L = \kappa\Delta/\lambda_b^2$ where λ_b is the thickness of the thermal BL, which scales as $\lambda_b/L \sim Nu^{-1}$. This leads to the well-known thermal–laminar boundary layer (BL) scaling

$$Nu = Re^{1/2}Pr^{1/2}, \tag{3.2}$$

and provides a relation tying Nu, Re and Pr. Noting that the thickness of the laminar boundary layer scales as $\lambda_u/L \sim Re^{-1/2}$, the scaling of the mean dissipation in the

https://doi.org/10.1017/jfm.2024.757 Published online by Cambridge University Press

Trial n^o	L	ρ_s	$\rho_{s,tank}$	ρ_f	$\rho_{f,tank}$	$\dot{Q}$	τ_{end}	$\tau_F \times 100$	τ_{end}/τ_F	Ra	Ra_f
1	0.5	1.0044	1.0053	0.9989	0.9980	10	4.5	3.00	150	5.46×10^{12}	2.27×10^{15}
2	0.5	1.0125	1.0140	0.9994	0.9981	10	5	2.56	195	1.19×10^{13}	3.65×10^{15}
3	0.5	1.0176	1.0209	1.0009	0.9981	10	5	2.38	210	1.71×10^{13}	7.70×10^{15}
4	0.5	1.0272	1.0322	1.0017	0.9980	10	4	2.19	182	2.55×10^{13}	1.10×10^{16}
5	0.5	1.0378	1.0580	1.0080	0.9981	10	5.5	1.97	281	4.48×10^{13}	3.80×10^{16}
6	0.5	1.0808	1.0915	1.0101	0.9984	10	4	1.79	222	6.96×10^{13}	2.83×10^{16}
7	1.21	1.0061	1.0072	0.9989	0.9982	40	13.5	4.08	331	9.54×10^{13}	5.32×10^{16}
8	1.21	1.0180	1.0206	1.0008	0.9982	40	14	3.40	412	2.37×10^{14}	1.54×10^{17}
9	2	1.0090	1.0097	0.9990	0.9982	80	16	4.57	337	5.51×10^{14}	2.42×10^{17}
10	2	1.0172	1.0209	1.0021	0.9981	80	15	4.14	362	1.09×10^{15}	1.24×10^{18}
11	2	1.0313	1.0320	1.0027	0.9984	80	17	3.83	443	1.61×10^{15}	8.74×10^{17}
12	2	1.0498	1.0580	1.0063	0.9981	80	16	3.41	468	2.87×10^{15}	2.65×10^{18}
13	2	1.0954	1.1010	1.0112	0.9981	80	18	3.06	587	4.93×10^{15}	3.02×10^{18}
14	4.87	1.0185	1.0214	1.0029	0.9986	160	28	5.91	473	1.57×10^{16}	1.38×10^{18}
15	4.87	1.0388	1.0452	1.0069	0.9981	160	25	5.11	489	3.25×10^{16}	2.91×10^{19}
16	4.87	1.0803	1.1010	1.0108	0.9982	160	27	4.37	617	7.11×10^{16}	8.30×10^{19}

Table 1. Summary of control and response parameters obtained from the wells of the experiment. Units for the length of the tank L are in (m), the density of the wells and tanks ρ (g cc^{-1}), pumps' flow rate $\dot{Q}$ (ml min^{-1}), duration of the experiment τ_{end} and the circulation overturn time τ_F (days). The total runtime sums to 201.5 days.

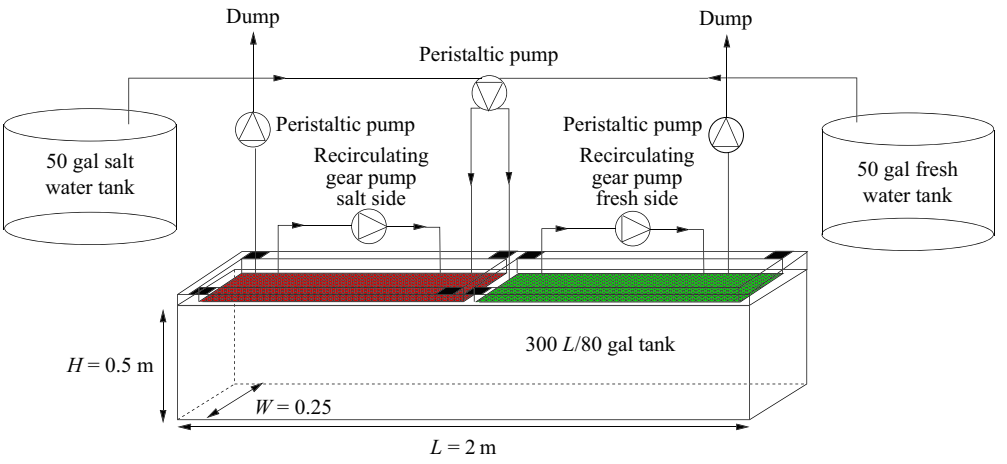

Figure 1. Schematics of the present set-up showing the tank with the fresh-water well on the right (green) and salt-water well on the left (red) set over the free surface and constantly stirred to maintain a uniform salinity in the well.

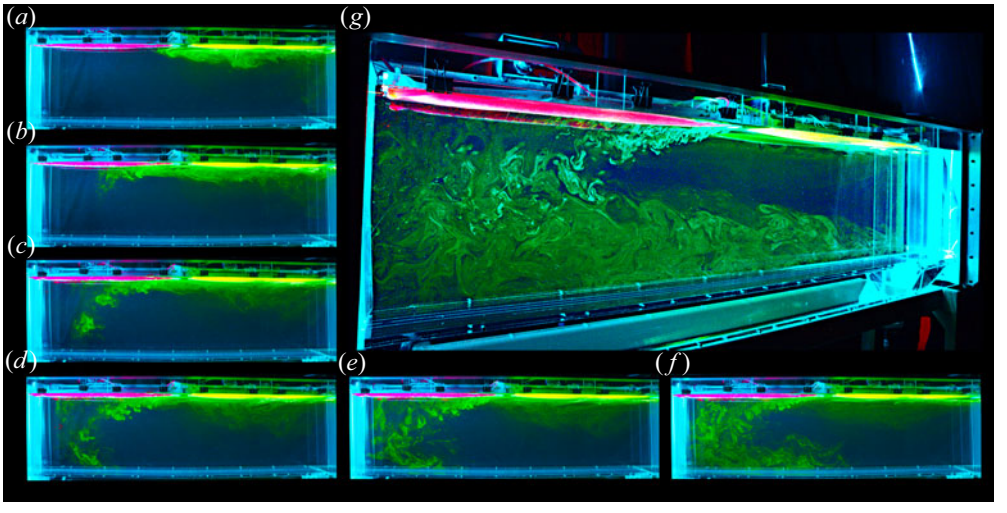

Figure 2. Side view of the tank, illuminated from the left and showing the evolution of fresh fluorescein dye water released from the right. The temporal evolution of the circulation is described by the transport of the fluorescein (green/yellow) dye, driven by a solutal horizontal density gradient, creating a turbulent plume sinking on the left of the tank (*a–f*). The deep circulation is shown in (*g*), where the flow has developed and drives a deep but weakly turbulent circulation that eventually upwells to the right of the tank. Reproduced from Passaggia *et al.* (2017).

particular case of laminar BL (Landau & Lifschitz 1987) is

$$\overline{\epsilon_{u,BL}} \sim \nu \frac{U^2}{\lambda_u^2} \frac{\lambda_u}{H} = \nu^3 H^{-4} Re^{5/2}. \tag{3.3}$$

Combining (3.2), (3.3) and (3.5), one recovers the laminar scaling (Rossby 1965, 1998; Gayen *et al.* 2014; Shishkina *et al.* 2016)

$$Re \sim Ra^{2/5} Pr^{-4/5}, \tag{3.4a}$$

$$Nu \sim Ra^{1/5} Pr^{1/10}. \tag{3.4b}$$

By analogy to the notation in the GL theory for Rayleigh–Bénard convection (RBC) (Grossmann & Lohse 2000; Shishkina *et al.* 2016), this scaling regime is denoted as I_l, where the subscript l stands for low-Pr fluids.

3.2. *The Paparella & Young (2002) inequality*

Both HC and RBC are closed systems driven by the buoyancy flux imposed through their boundaries. Paparella & Young (2002) (PY here and hereafter) first performed a spatio-temporal average of the kinetic energy equation, leading to the equality

$$\overline{\epsilon_u} = \overline{wb}, \tag{3.5}$$

where $\overline{\epsilon_u}$ is the mean kinetic energy dissipation rate $\overline{\epsilon_u} \equiv \nu \sum_{i,j} (\partial u_j/\partial x_i)^2$. Averaging the buoyancy equation in time and along horizontal planes requires

$$\langle wb \rangle = \kappa \partial \langle b \rangle / \partial z, \tag{3.6}$$

where $\langle \cdot \rangle$ denotes the time and horizontal average and the integration constant is zero because, at steady state, the horizontally averaged fluxes at the boundaries must add up to zero. Finally, vertical integration of the last equation leads to

$$\overline{wb} = \kappa (\langle b \rangle_{z=H} - \langle b \rangle_{z=0})/H = B(\Gamma/2)\kappa \Delta / L, \tag{3.7}$$

where $0 < B < 1$ is an arbitrary constant because, in the fluid, buoyancy differences cannot exceed the difference imposed at the boundary. The PY inequality thus writes

$$\overline{\epsilon_u} = B(\Gamma/2)\nu^3 L^{-4} RaPr^{-2}, \tag{3.8}$$

which, combined with the original idea of Rossby, opens possibilities for relating the dissipation in the boundary layer or the core with the heat transfer coefficient near the horizontal boundary.

An interesting consequence is that, as Ra increases while keeping Pr and Γ constant, the flow becomes progressively confined under the conducting boundary. This effect is also known as the anti-turbulence theorem and implies that, beyond a certain point, the overturning depth scale becomes

$$h < H, \tag{3.9}$$

and a stratified fluid zone that is nearly quiescent will form on the insulating boundary adjacent to the conducting horizontal boundary. Note that Shishkina *et al.* (2016) refer to h as the large-scale overturning flow in their analysis.

This is also what Sandström (1916) inferred from his experiments, that is, at large Ra, or high Pr, the flow becomes confined to a progressively thinner surface layer and the core becomes a stagnant pool of stratified water (Defant 1961). Although such regimes were only observed in direct numerical simulations of laminar HC (Ilicak & Vallis 2012) at high Pr and theoretically by Chiu-Webster *et al.* (2008) for the same regimes, experiments by Wang & Huang (2005) show the onset of this behaviour at intermediate Pr and intermediate Ra.

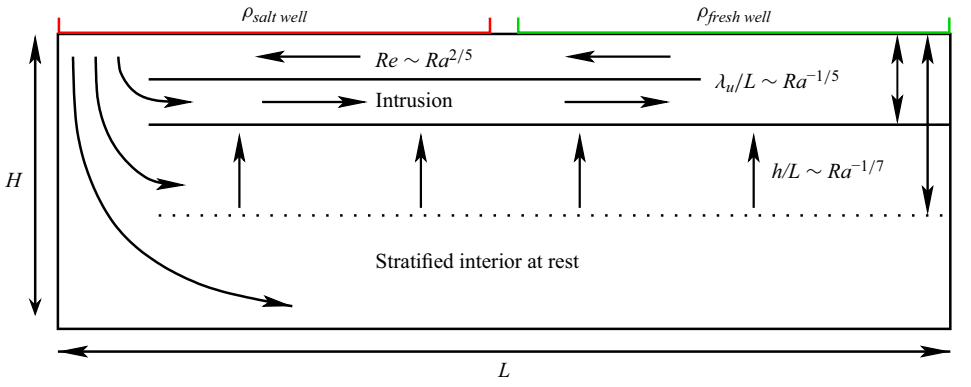

Figure 3. Schematics showing the intrusion regime of Chiu-Webster *et al.* (2008) and the scaling exponents reported in the present study. Note that the Hughes *et al.* regime would correspond to $h = H$ and the intrusion flow scale to $\lambda_b/L \sim Ra^{-1/5}$ while the Rossby regime would correspond to $\lambda_u \approx H$.

As Ra and/or Pr increase, the Rossby regime can no longer hold, since the thickness of the return flow decreases as $\lambda_u \sim Ra^{-1/5}$ for increasing Ra and $\lambda_b \sim Pr^{-1/10}$. In other words, the circulation clusters underneath the forcing boundary, which leads to two different regimes, as explained in the next subsections.

3.3. *The Chiu-Webster intrusion regime at high Prandtl numbers*

Chiu-Webster *et al.* (2008), building on the work of Rossby (1965, 1998), posited that HC is not sensitive to the type of boundary condition (free slip or no slip) applied to the velocity field. In addition, they hypothesized that the plume dynamics should depend on the Prandtl number. While the scaling for the heat and momentum transfer remains essentially the same as Rossby's work, these authors showed that the flow has a more complex structure, characterized by three distinct regions:

(i) A narrow intrusion, clustered underneath the forcing boundary of thickness $\lambda_b/L \sim Ra^{-1/5}$.
(ii) A strongly stratified interior where the fluid is at rest and whose thickness scales as $h/L \sim Ra^{-1/7}$.
(iii) The plume connecting the intrusion layer and the stably stratified interior.

The structure of the flow is depicted in figure 3.

3.4. *Hughes et al.'s (2007) laminar boundary-layer/turbulent plume regime* I_u^+

Increasing Ra and for intermediate Pr, the momentum boundary layer becomes progressively thinner compared with the thermal boundary layer. In this case, it is the thermal boundary layer that drives the dynamics and leads to a turbulent plume and a circulation that spans the entire depth of the domain. This particular case was theorized by Hughes *et al.* (2007) with a plume model inside a filling box. Here, we recast their model according to the Shiskina–Grossmann–Lohse (SGL) theory (i.e. see the plume model definition (2.15)–(2.20) in Hughes *et al.* 2007) and the dissipation in the boundary layer is balanced by the ratio between the thermal and momentum boundary layers λ_b/λ_u

according to

$$\overline{\epsilon_u}_{HGMP} \sim \nu \frac{U^2}{\lambda_u^2} \frac{\lambda_u}{H} \frac{\lambda_b}{\lambda_u} = \nu^3 H^{-4} Re^{5/2} Pr^{-1/2}, \tag{3.10}$$

where the dissipation now scales with the thickness of the thermal layer and is given by $\overline{\epsilon_u} \sim \nu U^2/(\lambda_b L)$. Combining (3.2), (3.8) and (3.10) we obtain

$$Re \sim Ra^{2/5} Pr^{-3/5}, \tag{3.11a}$$

$$Nu \sim Ra^{1/5} Pr^{1/5}. \tag{3.11b}$$

Such a regime is denoted as I_u^+ and was first observed in the experiments of Mullarney *et al.* (2004) and Wang & Huang (2005), and later confirmed in the direct numerical simulations of Gayen *et al.* (2014).

3.5. *The Shishkina & Wagner (2016) laminar regime I_l^**

At low Ra and for large Pr and/or large aspect ratio Γ, the thickness of the momentum boundary layer λ_u extends over the depth of the domain, giving $\lambda_u = H$. The relation (3.5) becomes

$$\overline{\epsilon_u}_{SW} \sim \nu \frac{U^2}{H^2} = \nu^3 H^{-4} Re^2. \tag{3.12}$$

This expression is equivalent to the dissipation of a pressure-driven laminar channel-type flow. Because this regime requires that the boundary layers span the entire domain, this flow may only be observed for high aspect ratio domains or small Rayleigh numbers, which enforce confinement and is the case in the present study. Combining (3.2), (3.8) and (3.12), we obtain the laminar scaling derived in Shishkina & Wagner (2016)

$$Re \sim Ra^{1/2} Pr^{-1}, \tag{3.13a}$$

$$Nu \sim Ra^{1/4} Pr^{0}, \tag{3.13b}$$

denoted as I_l^*, where Beardsley & Festa (1972) first attempted numerical simulations. It is interesting to note that this scaling is similar to the analysis of Gramberg *et al.* (2007) in which the return flow takes place along the bottom layer and may be applicable when the boundary layer spans the entire height of the domain. Note that Rossby (1998) also observed a steeper scaling than $Nu \sim Ra^{1/5}$ in his numerical simulations for low Ra (see p. 248 in Rossby 1998) and similarly in the work of Siggers, Kerswell & Balmforth (2004).

Note that the Shishkina & Wagner (2016) regime I_l^* is expected to occupy the full depth of the domain in figure 3 and we anticipate that the intrusion regime will occur for a larger Ra than the I_l^* regime.

3.6. *The role of the aspect ratio and finite width*

The effect of the domain aspect ratio was also analysed by Chiu-Webster *et al.* and was reanalysed by Sheard & King (2011), who reached similar conclusions: for small aspect ratios $\Gamma < 1$ and large enough Rayleigh numbers, the flow follows the I_l regime. For $\Gamma \geqslant 2$ and $Pr \gg 1$, the Nusselt-number dependence exhibits a slightly steeper scaling and agrees with the conclusions of Shishkina & Wagner. Note that these theories did not consider the effect of sidewalls and thus the importance of finite or closed domains. This particular point remains an open question and will not be addressed in this work.

3.7. *Turbulent regimes at high Prandtl numbers*

Most of the existing work in HC at high Pr considers flows driven by laminar-type scaling laws, dominated by the behaviour of the boundary layer, except for an analogue of HC by Griffiths & Gayen (2015) and Rosevear *et al.* (2017). In a recent study, they considered a spatially periodic forcing at the conducting boundary with a short wavelength compared with the depth of the domain. Part 1 identifies a similar transition, but the present study could not achieve the necessary Rayleigh numbers (up to Ra^{22}) to allow us to observe the transition to a such regime.

4. Experimental results

4.1. *Time-scale analysis*

We begin by considering the time scale over which a high-Pr HC system will reach a steady state. Clearly, such experiments are possible if the actual time scale is considerably shorter than the purely diffusive time $\tau_d \sim \kappa^{-1}H^2$, which is close to a year for the largest tank used in our experiments. As we shall see, convection considerably shortens the transient by stirring the top layer or by entrainment and detrainment in the plume, as seen in figures 2 and 3. The amount of buoyancy transported along the horizontal direction over the distance L is controlled by the streamfunction Ψ and the thickness of the pycnocline. Using the scaling laws derived in the previous section,

$$\Psi_{max}/\kappa \sim Ra_f^{1/6} \quad \text{and} \quad \lambda_b/L \sim Ra_f^{-1/6}, \tag{4.1a,b}$$

and substituting relation (2.3) together with the definitions of the Nusselt and the Reynolds number, the scaling laws become

$$Re \sim \Psi_{max}/\kappa \approx c_1 Ra^{1/5} \quad \text{and} \quad Nu \sim (\lambda_b/L)^{-1} = c_2 Ra^{1/5}. \tag{4.2a,b}$$

The prefactors c_1 and c_2 are obtained fitting the theory from experimental data. In this HC set-up, Griffiths *et al.* (2013) showed that the stable layer acts as a buffer to adjustments or imbalances imposed at the boundaries. In the stably stratified region, the conductive flux is the only mediator to mass, and thus buoyancy transfers. In the case of an imposed buoyancy flux, the initial state has an interior buoyancy b_1 and a total buoyancy flux input $Q_1 = F_1 WL/2$ through the membrane with the denser fluid located above the tank. In the initial steady state, the flux withdrawn is equal to the input Q_1. Consider the case of a flux boundary condition (Neumann). At $t = 0$ let the negative buoyancy input increase from Q_1 to $Q_2 = Q_1 + \delta Q$. Previous experiments and numerical solutions show that the boundary buoyancy input in the equilibrium state is carried to the bottom of the tank by the endwall plume (shown in figure 2, see also Mullarney *et al.* 2004; Stewart *et al.* 2012; Gayen *et al.* 2013; Passaggia *et al.* 2017). Therefore, we can assume that, in the transient flow, the 'unbalanced' buoyancy input (in excess of that in the equilibrium state) will also be carried to the bottom of the domain by the plume, where it spreads laterally across the bottom of the tank before being displaced upward by the continuing plume transport. Thus, the interior buoyancy $b(t)$ decreases, leading to an increase in buoyancy difference $b - b_f$ across the boundary layer and an increasing rate of conductive negative buoyancy withdrawal, which we write as $Q = Q_1 + Q_0(t)$. The rate of change in buoyancy $\tilde{b}$ averaged over the interior assuming that $\lambda_b \ll H$ obeys

$$LWH\frac{\mathrm{d}\tilde{b}}{\mathrm{d}t} = \delta Q - Q'(t), \tag{4.3}$$

where $\tilde{b}(t)$ is the spatial average of the buoyancy over the domain. The imbalance vanishes at large times, when $Q'(t) \to \delta Q$. For quasi-steady conduction in the boundary layer over the buoyant half-part of the top, the rate of buoyancy withdrawal is

$$Q_1 + Q'(t) \approx \beta\kappa \left(\tilde{b} - b_f\right) LW/2\lambda_b, \tag{4.4}$$

over the half of the domain $L/2$ and we write the gradient at the boundary as $\langle \mathrm{d}b/\mathrm{d}z\rangle_{z=H} \approx \beta(\tilde{b} - b_f)/\lambda_b$ (the factor 2 stems from the fact that freshening occurs only over half of the domain). In their analysis, Griffiths *et al.* (2013) did not separate the momentum BL (λ_u) from the buoyancy (thermal in their case) BL (λ_b) and defined β so that 95 % of the overall buoyancy difference lies in the BL. The constant was evaluated from direct numerical simulation (DNS) for $\beta \approx 1.4$ at $Pr \approx 5$. Since the flow is essentially laminar in the stably stratified layer and transitional in the statically unstable zone, the constant β can be seen as the ratio between the momentum BL and the buoyancy BL such that

$$\beta \approx \frac{\lambda_u \langle \mathrm{d}b/\mathrm{d}z\rangle_{z=H}}{(\tilde{b} - b_f)} \approx c_4 \lambda_u Nu \approx c_4 Re^{-1/2} Nu \approx c_4 Pr^{\alpha}, \tag{4.5}$$

where $\alpha = 1/2$ in the Rossby and Shishkina & Wagner regimes while $\alpha = 4/10$ for the Hughes' *et al.* regime. Applying the above to the results of Griffith *et al.*, we obtain $c_4 \approx 0.74$, while $c_2 \approx 0.71$ was obtained from figure 4. At large time, the system approaches the final equilibrium state, in which $\tilde{b} = b_2$ and

$$Q_1 + \delta Q \approx \beta\kappa \left(b_2 - b_f\right) LW/2\lambda_b. \tag{4.6}$$

Taking λ_b as constant for small changes in boundary conditions and combining (4.3)–(4.4) gives the interior buoyancy

$$\tilde{b} \approx b_1 + \delta b \left(1 - \exp(-\beta\kappa t/2\lambda_b H)\right), \tag{4.7}$$

which exponentially approaches a final equilibrium temperature b_2, the magnitude of the resulting change being

$$\delta b = b_2 - b_1 = 2\lambda_b \delta Q/\left(\beta\kappa LW\right) = \lambda_b \delta F/\left(\beta\kappa\right). \tag{4.8}$$

In normalized form, the deviation from the final equilibrium is

$$\mathcal{B} = \left(\tilde{b} - b_2\right)/\left(b_1 - b_2\right) \approx \exp(-\beta\kappa t/2\lambda_b H). \tag{4.9}$$

The imposed flux condition causes the box to equilibrate to the new conditions on the exponential time scale $\tau_F \approx \beta\lambda_b H/\kappa$. The Rayleigh-number scaling (4.2*a*,*b*) justifies our assumption of constant λ_b for modest changes in boundary conditions. It also implies a more rapid adjustment for larger Ra_f such that

$$\kappa\tau_F/H^2 \approx (2/\beta)(\lambda_b/H) \approx \Gamma\,(2c_2/c_4)\, Ra^{-1/5} Pr^{-1/2}. \tag{4.10}$$

The evolution of Ra_f (or equivalently Nu) in each well is shown in figure 5, where both the source and the sink of buoyancy reach the same value, which implies that the flow has reached a steady state and that no significant evaporation is taking place. Note that the time scale was not non-dimensionalized to reflect the duration of the experiments in different tanks. For example, in the small tank, the diffusion time scale for salt $\tau_d \sim \kappa^{-1}H^2 \approx 5$ days, while in the largest tank, it would be nearly one year. Although four

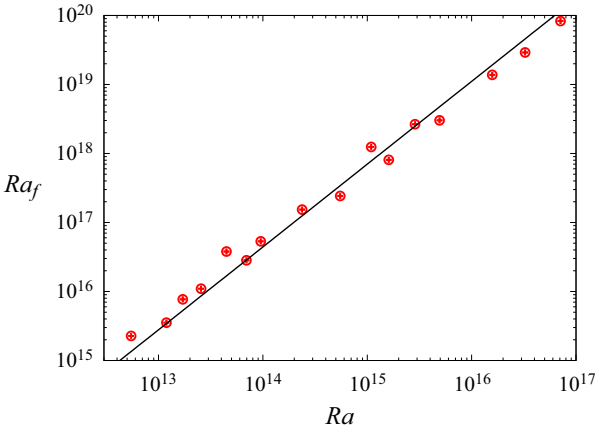

Figure 4. Flux-Rayleigh number Ra_f as a function of Ra plotted against the laminar scaling $Ra_f \approx c_2 Ra^{6/5}$ where $c_2 = 0.71$.

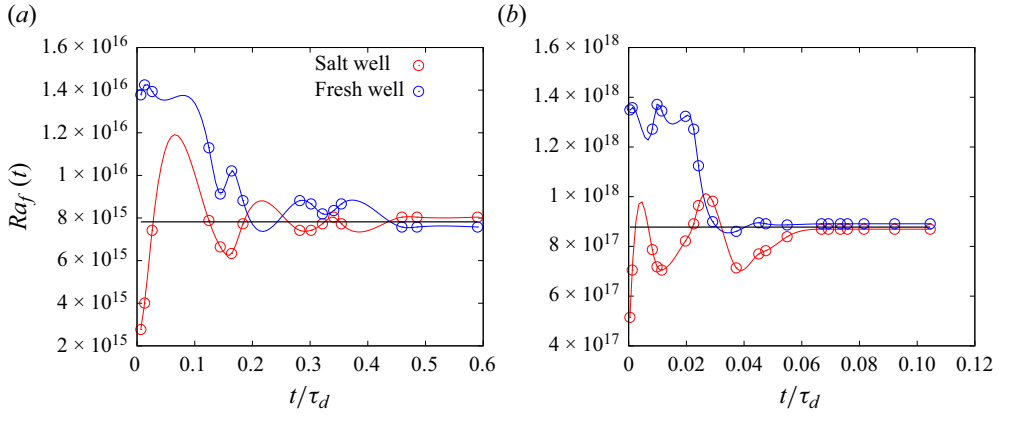

Figure 5. Temporal evolution of the flux-Rayleigh value in the small tank $L = 0.5$ m (a) and the medium tank $L = 2$ m (b) over time. Here, time is rescaled with respect to the diffusion time scale τ_d. Blue curves represent the evolution of fresh-water wells, and red curves represent the evolution of salt-water wells.

days are necessary to obtain a steady state in the small tank, which already suggests that a viscous scaling will be at play, it only took a month to reach a steady state in the larger tank, confirming that vigorous convection at the surface is present. Under the conditions of the experiments reported in this paper, we find $\kappa\tau_F/H^2 \approx [9.7, 201] \times 10^{-3}$ (or $\tau_F \approx [1.2 \times 10^3, 5.1 \times 10^3]$s). Sample results are shown for the $L = 0.5$ m tank in figure 5(a) and for the $L = 2$ m tank in figure 5(b) where all cases were run for at least 100 times the flux time scale τ_f highlighted in the analysis. Note that τ_f was also used to estimate the time it would take between the time the particles were inserted and the collection of PIV data.

As suggested by Rocha *et al.* (2020), this time scale may prove to be short compared with the actual time necessary to establish a complete steady state, since the bulk and the boundary layers may be characterized by different time constants. In their numerical simulations, they found that a complete steady state was achieved for a time scale $\tau \approx 0.15\tau_d$. Note that these experiments were in a transitional regime at $Pr = 1$ and that our

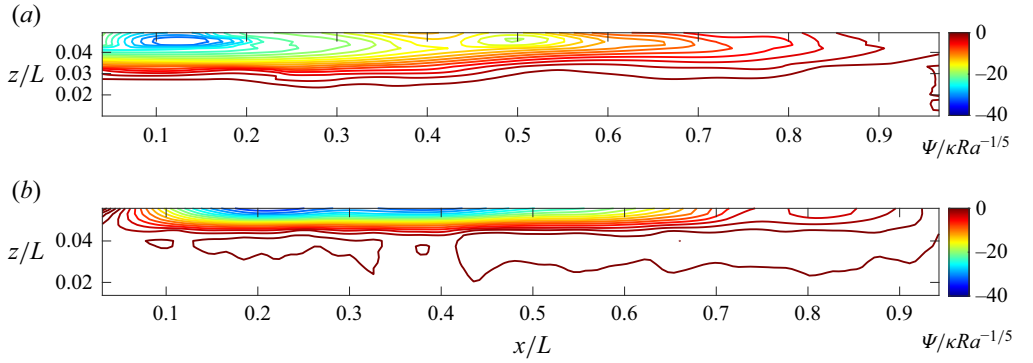

Figure 6. Snapshots of the mean streamfunction for (*a*) $Ra = 1.19 \times 10^{13}$ and (*b*) $Ra = 4.48 \times 10^{13}$ corresponding to trials 2 and 5 in table 1 showing the progressive clustering of the circulation beneath the forcing boundary. These figures were obtained from PIV, integrating the mean velocity to obtain the streamfunction Ψ, which is then non-dimensionalized using (4.2*a*,*b*).

experiments were carried out until the measured fluxes were balanced (at least $0.15\tau_d$), confirming that steady states were reached for each experiment.

4.2. *Steady states and local measurements*

The PIV of the full domain could only be performed for the smaller tanks, and we resorted to another alternative to estimate the Reynolds and Péclet numbers for the larger tanks. Since we work in tanks with a large aspect ratio (i.e. $\Gamma = 16$), we propose an estimate for the Reynolds number, which can be obtained from measurements of the local streamfunction in the middle of the domain. At first order, the Reynolds number is approximated as

$$Re \approx \frac{L^2}{H\lambda_u \nu} \max(\Psi(z))|_{x=L/2,y=W/2}, \tag{4.11}$$

where the lateral effects were neglected. The Péclet number can then be defined as $Pe = PrRe$. This is consistent with our experimental observation of the streamfunction measured with PIV (figure 6*a*).

Rescaled density profiles, measured in the centre of the domain $x = L/2$ are shown in figure 7(*a*) for most of the range of Rayleigh numbers reported in the present study. As Ra increases, the flow exhibits the same behaviour as seen in the experiment of Mularney *et al.* but with a thinning of the pycnocline and an increase in the dense, well-mixed fluid, filling the bottom and the centre of the domain.

The profiles of the streamfunction normalized with the Rossby scaling and collected at the same location are shown in figure 7(*b*) for the same values of Ra as in figure 7(*a*). The two regimes identified with the analysis of the Nusselt-number scaling can also be observed with the evolution of the streamfunction as a function of Ra. The maximum of the streamfunction becomes progressively closer to the forced boundary at $z = H$. It should be noted that the location of the streamfunction approaches the buoyancy–forced boundary when $Ra \gtrsim 10^{15}$ while the flow is essentially at rest in the core of the domain. This observation follows the results of the experiments of Wang & Huang (2005) performed at $Pr \approx 8$. Note that Wang & Huang also reported a regime transition, but did not see a change in exponents across each regime. We emphasize that, in the case of Wang & Huang, the aspect ratio was small $\Gamma = 1.3$ and of width $W/L \approx 1/8$, while in our experiments

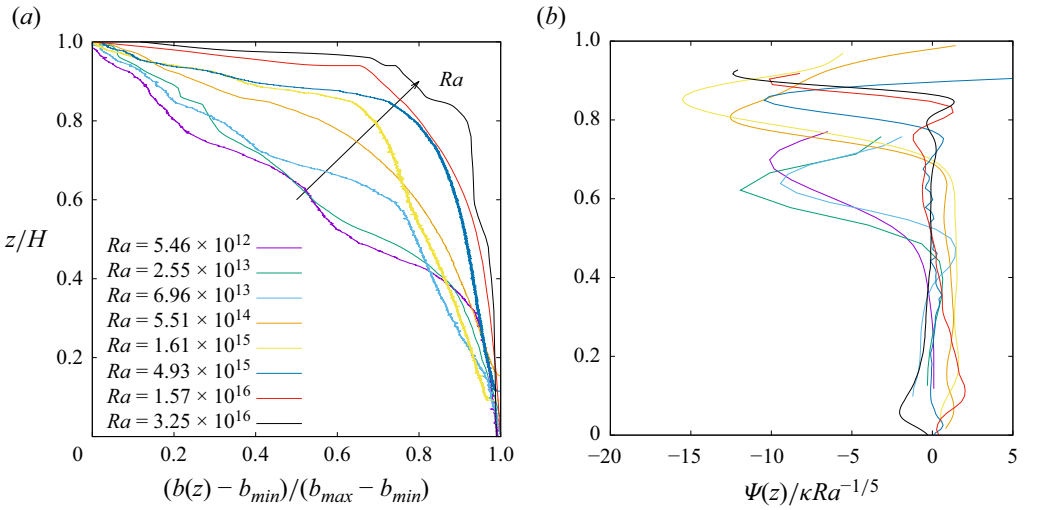

Figure 7. (*a*) Normalized density profiles $(\rho(z) - \rho_{min})/(\rho_{max} - \rho_{min})$ and (*b*) streamfunction $\Psi(z)$ non-dimensionalized using (4.2*a*,*b*) and calculated from averaged PIV data and rescaled with Rossby scaling as suggested by Chiu-Webster *et al.*, measured in the middle of the tank ($x = L/2$).

$\Gamma \approx 16$ and $W/L \approx 1/16$. We therefore witness the transition from a confined flow to the flow with an interior at rest, as recently described in Shishkina & Wagner (2016). Note that a small recirculation region is observed in figure 7(*b*) at the bottom of the tank (shown by a small bump in the streamfunction), which was present in almost all experiments except for the smaller tank. We hypothesize that this feature, not present in the Wang & Huang experiments, is possibly due to undesirable heating from the bottom of the tank.

Chiu-Webster *et al.* (2008) derived asymptotic solutions to the problem of very viscous convection, and in particular, the solution for the evolution of the temperature in the core of the domain. In particular, they showed that the temperature (i.e. equivalent to the buoyancy up to a negative multiplicative constant) scaled as

$$b(z) = \frac{c_5}{Ra(z+h)^7}, \tag{4.12}$$

where h is the height of the bulk as defined in figure 3 and c_5 is a constant, both obtained from fitting the results in figure 7(*a*) to (4.12). As shown in Chiu-Webster *et al.*, the height h derives naturally at first order for the temperature equation in the limit where $Pr \to \infty$, which becomes Laplace equation in this particular limit. Using the results obtained in figure 7(*a*), figure 8(*a*) shows that self-similarity can be recovered in the interior and that $b(x = L/2, z) \approx c_5(z + h)^{1/7}$ where $c_5 = 1.9$.

Figure 8(*b*) shows the values of the streamfunction obtained in 7(*b*) rescaled with $Ra^{1/5}$ for the vertical direction z as in (4.2*a*,*b*), and for a large range of Rayleigh numbers. It is worth noting that the streamfunction becomes self-similar in the range $(1 - z\Gamma)Ra^{1/5} = [0, 1]$ and $Ra > 10^{15}$, which corresponds to circulating flow. Note that the solution is no longer self-similar where $(1 - z\Gamma)Ra^{1/5} > 1$, which justifies the use of (4.12) in the interior, providing further support for the analysis of the regime transitions.

4.3. *Scaling analysis*

The dependence of Nu and Ψ_{max} (and equivalently Re) on the Rayleigh number Ra is summarized in figure 9(*a–f*). Similarly to the analysis in terms of the flux–Rayleigh

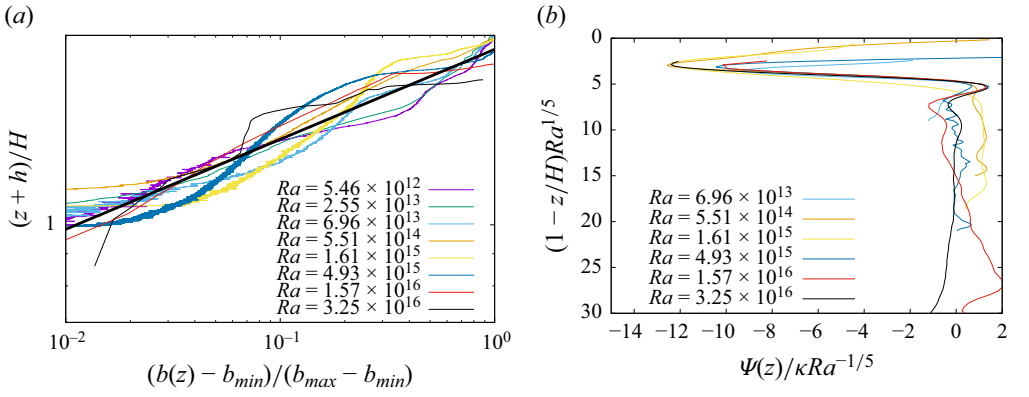

Figure 8. (*a*) Rescaled normalized buoyancy profiles as defined in (4.12). (*b*) Rescaled streamfunction profiles showing the self-similar nature of the flow near the upper boundary.

number, we observe two different scaling exponents (figure 9*a*): for $Ra \lesssim 10^{15}$, the flow exhibits a scaling exponent $Nu \sim Ra^{1/4}$, while for $Ra \gtrsim 10^{15}$ the salt uptake rate decreases to exhibit a $Nu \sim Ra^{1/5}$-type scaling. The same compensated plot is shown in figure 9(*b*), where the difference between the two scalings is only a factor 2.5 at $Ra = 7.11 \times 10^{16}$ over the full dynamic range of our experiments and underlines the importance of the large Rayleigh-number ranges to differentiate between the two scaling laws.

Based on figure 7(*a*,*b*), we extrapolate the thickness of both the kinetic boundary layer λ_u and the pycnocline thickness λ_b. The former is given by the location of the maximum of the streamfunction $\max(\Psi(z))$, the latter was extrapolated using the height of the fiftieth percentile of the rescaled density profile. The evolution of the buoyancy boundary layer is reported in figure 9(*c*) and shows again two different behaviours. For $Ra < 10^{15}$, the buoyancy boundary-layer thickness decreases and follows a $Ra^{-1/4}$ scaling. At $Ra \approx 10^{15}$, we observe a regime change where the thickness now decreases so that $Ra^{-1/4}$. A similar behaviour is observed in figure 9(*d*), where the thickness of the kinetic boundary layer λ_u is reported. For $Ra \lesssim 10^{15}$, the kinetic boundary layer saturates at $\lambda \approx 0.4$, which is in agreement with the study of Shishkina & Wagner (2016). Past $Ra \gtrsim 10^{15}$, we recover the Rossby scaling for $\lambda_u \sim Ra^{-1/5}$ and, together with the bulk reduction, this suggests that we are observing the intrusion-type flow studied by Chiu-Webster *et al.* (2008).

We confirm this claim in figure 9(*e*), where the thickness of the core $h\Gamma$ is shown as a function of the Rayleigh number. This thickness was measured fitting (4.12) from the data reported in figure 7(*a*), as shown in 8(*a*). Using their plume theory, Chiu-Webster *et al.* (2008) showed that the thickness of the bulk decreases as $Ra^{-1/7}$. This scaling is compared with the data points that suggested such behaviour for $Ra \gtrsim 10^{15}$. Although based only on a few data points, we may be witnessing the intrusion regime described by Chiu-Webster *et al.* (2008).

Conclusions from the maximum of the streamfunction shown in figure 9(*f*) are more difficult to draw. From Shishkina & Wagner (2016), we would expect a Reynolds-number scaling as $Re \sim Ra^{1/2}$ and $\lambda_u \sim Ra^{1/2}$, which results in $\Psi_{max} \sim Ra^{1/4}$. For larger values of Ra, we would expect $\Psi_{max} \sim Ra^{1/5}$, similar to the Rossby scaling. A linear regression across the entire data set provides $\max \Psi \sim Ra^{0.225}$, which lies between the 1/4 exponent expected from the Shishkina & Wagner (2016) analysis and the 1/5 predicted in Chiu-Webster *et al.* (2008). Note that all data points for the maximum of

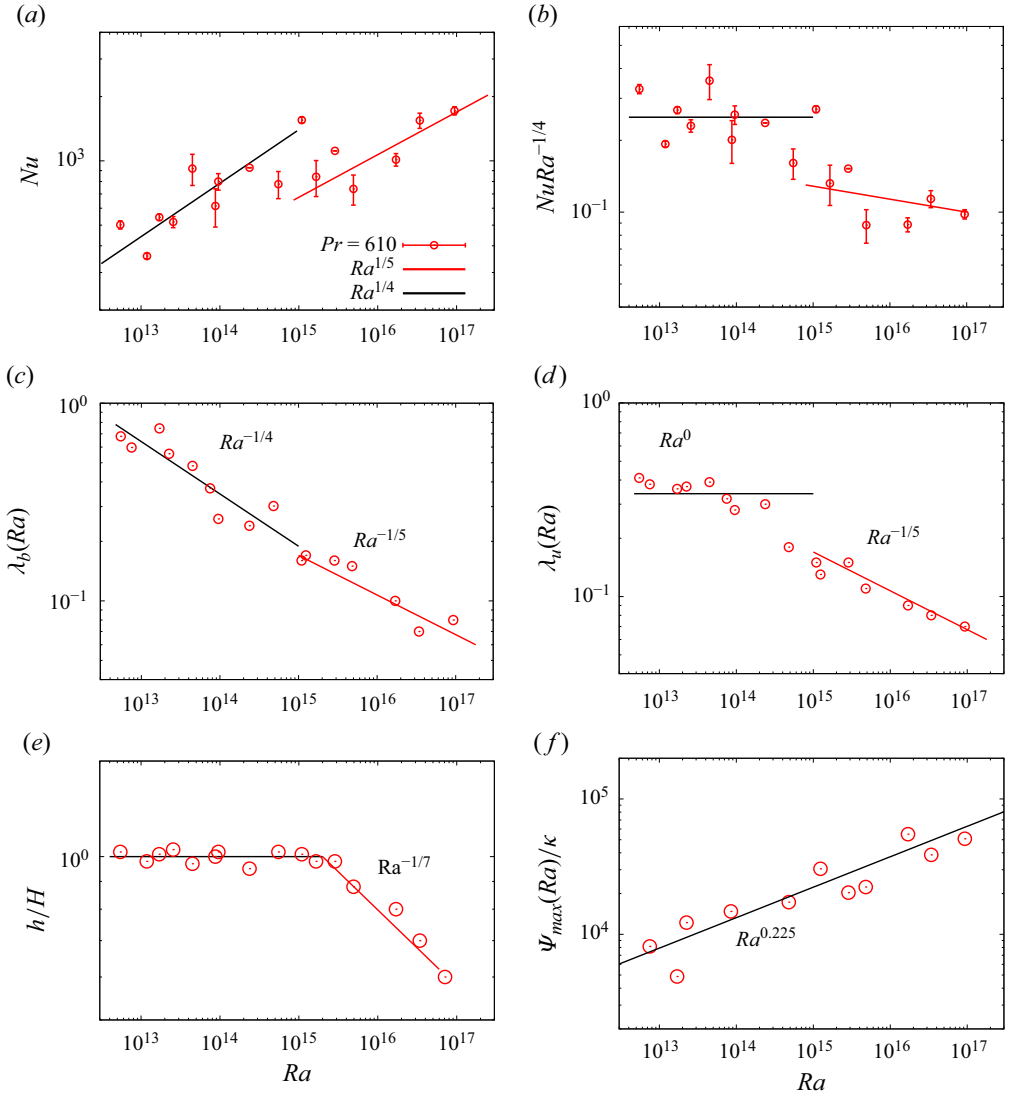

Figure 9. The (*a*) *Ra* and (*b*) rescaled-*Ra* dependencies of the Nusselt number. (*c*) Buoyancy boundary-layer thickness λ_b and (*d*) momentum boundary thickness λ_u, compared with the theory of Chiu-Webster *et al.* (2008) (red) and Shishkina & Wagner (2016) (black). (*e*) Bulk thickness h/H compared with the theory of Chiu-Webster *et al.* (*f*) Maximum of the streamfunction Ψ_{max} as a function of *Ra* and the linear regression over the full range.

the streamfunction were not reported since PIV proved difficult near the boundary for the largest buoyancy inputs in the wells, in particular in the smaller tank.

The present experimental results, based on a regime similar to Shishkina & Wagner (2016), suggest a transition from the I_l^* regime to the I_u intrusion regime of Chiu-Webster *et al.* (2008) for Prandtl numbers one order of magnitude larger than the direct numerical simulations of Shishkina & Wagner (2016) and Rossby (1965), and Rayleigh numbers up to seven orders of magnitude larger than previous experiments and direct numerical simulations for similar Prandtl numbers. In the next subsection, we discuss the present

results with the results at intermediate and low Prandtl numbers presented in Part 1 We propose an updated regime transition diagram of horizontal convection.

5. Completing the regime diagram of natural horizontal convection

In this section, we summarize the different HC regimes that were observed in the (Ra, Pr) space in the present work and Part 1 (Passaggia & Scotti 2024), together with all the results that we could gather from the literature on HC (figure 10(a)–(b)). This section aims at extending the regime diagram in Hughes *et al.* (2007) and the limiting regimes provided in Shishkina *et al.* (2017).

We first provide a nomenclature for the different regimes:

(i) $\boxed{0}$ nearly conducting (i.e. $Nu \sim$ const.);
(ii) $\boxed{I}$ laminar;
(iii) $\boxed{II}$ transitional (only turbulent in the plume);
(iv) $\boxed{III}$ enhanced transitional (only turbulent in the BL but never observed);
(v) $\boxed{IV}$ both boundary layers and plume are turbulent.

Additional subscripts and superscripts are identified as:

(i) $\boxed{u}$ for large Prandtl numbers;
(ii) $\boxed{l}$ for low Prandtl numbers;
(iii) $\boxed{*}$ when essentially controlled by the aspect ratio;
(iv) $\boxed{+}$ when essentially controlled by the plume dynamics.

We begin with the conducting regime $\boxed{0}$, which was analysed in Siggers *et al.* (2004), Chiu-Webster *et al.* (2008) and, more recently, by Sheard & King (2011), where $Nu \sim Ra^0 Pr^0$. The onset is independent of the Prandtl number, the transition is smooth and weakly affected by the aspect ratio Γ and occurs when $Ra \approx 10^3$. The conducting regime neighbours the $\boxed{I_l^*}$ regime which follows the scaling in (3.12a) or the $\boxed{I_l}$ regime in (3.4a) depending on the aspect ratio. The transition was found to not depend on Ra, consistent with the results reported in the literature (Siggers *et al.* 2004; Sheard & King 2011).

The connection between the laminar regimes $\boxed{I_l^*}$ and $\boxed{I_l}$ is determined by matching the Reynolds numbers in these neighbouring regimes. From (3.12b) and (3.4b), we obtain the slope of the transition region between the regimes I_l^* and I_l, which is $Pr \sim Ra^{1/2}$. This transition is smooth (Shishkina *et al.* 2017), but is strongly affected by both the aspect ratio of the domain and the type of boundary conditions. Note that the free-slip boundary conditions make it easier to observe this regime. Results from Rossby (1998), Shishkina & Wagner (2016) and the present work confirm that high aspect ratio domains are necessary to observe the I_l^* regime. With increasing aspect ratios, the boundary layer becomes increasingly thick with respect to depth H and eventually covers the entire depth of the domain for a small enough Rayleigh number. To reflect this dependence in the regime diagram, this transition is marked by a dashed line because of its strong aspect ratio dependence. The present dashed line was approximated as a fit from the present results and Shishkina *et al.* for aspect ratios $\Gamma \sim O(10)$ but the reader should keep in mind that the present landscape should include a third dimension, Γ, to be complete.

As both Ra and Pr increase, the Rossby regime progressively evolves towards the intrusion regime studied by Chiu-Webster *et al.* (2008) and observed for large Rayleigh numbers in this study. This regime has the same dependence on the Prandtl and Reynolds numbers as the laminar Rossby regime, but the flow has a significantly different structure. We therefore propose to name this flow $\boxed{I_u}$ to remain consistent with the Shishkina *et al.* (2016) nomenclature.

As Ra increases and for $Pr \approx O(1)$, we observe the $\boxed{I_u^+}$ regime of Hughes *et al.* (2007). As shown in Gayen *et al.* (2014), the transition for increasing Ra is not smooth, and this flow exists only over a small region of the regime diagram. The flow transitions to $\boxed{I_u}$ when Pr increases and appears at constant Pr. This can be shown by equating (3.4*b*) and (3.10*b*) and this transition from $\boxed{I_u^+}$ to $\boxed{I_u}$ was highlighted by Gayen *et al.* (2014) (see p. 712).

For low Pr, a sharp transition from $\boxed{I_l}$ to $\boxed{II_l^*}$ was reported in Passaggia & Scotti (2024). This transition occurs at $Pr \sim Ra^{1/2}$ across a bifurcation of the flow. Note that, similarly to the high-Pr regimes, the circulation shrinks as Pr decreases. Also, note that the transition from $\boxed{II_l^*}$ to $\boxed{I_u^+}$ has a complex shape and is strongly dependent on the aspect ratio Γ.

The last transition appears as the Rayleigh number increases and was first observed at $Ra \approx 10^{11}$ and $Pr \approx 0.1$. The $\boxed{II_l^*}$ regime transitions to the limiting regime $\boxed{IV_u}$. This transition was smooth and marks the appearance of a first limiting regime for asymptotic Ra, consistent with the zeroth law of turbulence where the Reynolds and Nusselt numbers are driven by turbulent-scaling arguments. The transition from $\boxed{II_l^*}$ to $\boxed{IV_u}$ appears as $Ra \sim Cst$ as reported in Passaggia & Scotti (2024). The separation between the regime's argument is more difficult to draw since we have not been able to identify the transitions between the regimes directly from previous works. In addition, regime $\boxed{IV_u}$ displays logarithmic Reynolds-number corrections for the Reynolds and the Nusselt number, which lead to the scaling $Pr \sim Ra^{1.66}\mathcal{L}(Re^{16})$, which is strongly dependent on the Reynolds number. This is not too surprising since transition to turbulence is expected to be Reynolds-number dependent (Lohse & Shishkina 2023). Furthermore, the Prandtl-number dependence on the log correction could not be verified in the work of Passaggia & Scotti (2024), which leaves questions open regarding the complete understanding of this flow regime and its transitions. Another alternative would be to use the values reported in table 2 and match the Nusselt number between $\boxed{I_u^+}$ and $\boxed{IV_u}$. Still, the scaling law depends again on the actual values of the Reynolds number and would provide, for this particular case, $Pr \sim Ra^{-0.115}$. Note that the same conclusion applies to the transition between $\boxed{I_u}$ and $\boxed{IV_u}$. For these reasons, the transitions region is shown by a red dashed line and remains a matter for further investigation. All the regimes summarized in the section are provided in table 2.

Regarding the ultimate regime $\boxed{IV_l}$ predicted in Siggers *et al.* (2004) and Shishkina *et al.* (2017), where $Nu \sim Ra^{1/3}Pr^{-2/3}$ and $Re \sim Ra^{1/3}Pr^{1/3}$, the bound on the Richardson number in the stratified boundary layer, derived in Passaggia & Scotti (2024), shows that

	Regime type	0	I_l^*	I_l	I_u^+	I_u	II_l^*	IV_u
$Nu \sim Re^{\alpha} Pr^{\beta}$								
	α	0	1/4	1/5	1/5	1/5	1/6	0.225*
	β	0	0	1/10	1/5	1/10	7/24	0.417*
$Re \sim Ra^{\gamma} Pr^{\delta}$								
	γ	0	1/2	2/5	1/3	2/5	2/5	1/3
	δ	0	−2/3	−1	−4/5	−1	−3/5	−1

Table 2. List of scaling laws obtained for the Nusselt- and Reyolds-number dependencies across different regimes. The prefactors and the scalings with an asterisk are estimated from the numerical simulations. All other exponents are derived from theoretical considerations.

this regime seems unattainable as long as the boundary is considered as perfectly flat (Lohse & Shishkina 2023), (i.e. for instance without roughness elements). This particular point deserves more investigation and whether such a regime can be attained is of utmost importance for geophysical applications. Nevertheless, in the present academic configuration assuming perfectly flat boundaries, the regime $\boxed{IV_u}$ seems to be the limiting regime attainable at very large Rayleigh numbers.

This updated regime diagram covers, to the best of our knowledge, all previous DNS and experimental studies performed on HC. The last regime observed at high Rayleigh numbers is a turbulent-dominated regime in the bulk, which satisfies the zeroth law of turbulence Shishkina *et al.* (2016). The resulting flow characteristics at high Rayleigh numbers and all Prandtl numbers are an intensified turbulent near-surface circulation which follows Sandström's original inference, Jeffrey's argument and the PY bound on dissipation. They argued that the flow generated by HC would result in an essentially stagnant pool of water with little to no flow in the core and an intensified turbulent circulation localized near the differentially heated boundary. Our results show that limiting regimes at all Prandtl numbers for large Rayleigh numbers inevitably lead to such a scenario.

6. Conclusions

This work considers laboratory experiments of HC at high Prandtl and high Rayleigh numbers. This work aims to explore a part of the regime diagram that has not yet been explored in previous studies. Related experimental work at high Prandtl numbers dates back to the original work Rossby (1965) and Miller (1968) more than half a century ago. Instead of differential heating, where increasing the Prandtl number is achieved by increasing the viscosity of the working fluid, we consider solutal convection and use a permeable dialysis membrane to allow for a mass/salinity flux through the forcing boundary while ensuring a no-flow/no-slip boundary condition in a high aspect ratio and narrow domain.

Experiments that span four orders of magnitude in the Rayleigh number while keeping the Prandtl number constant are performed. This allows for measuring two known regimes, already identified in the literature in natural HC at higher Prandtl numbers but for much larger values of the Rayleigh number (up to seven orders of magnitude larger) than previously reported. We provide experimental evidence of the laminar regime identified by Shishkina & Wagner (2016) where the recirculating flow, and thus the boundary layer, has the same domain size. This regime leads to a regime $Nu \sim Ra^{1/4}$ that is

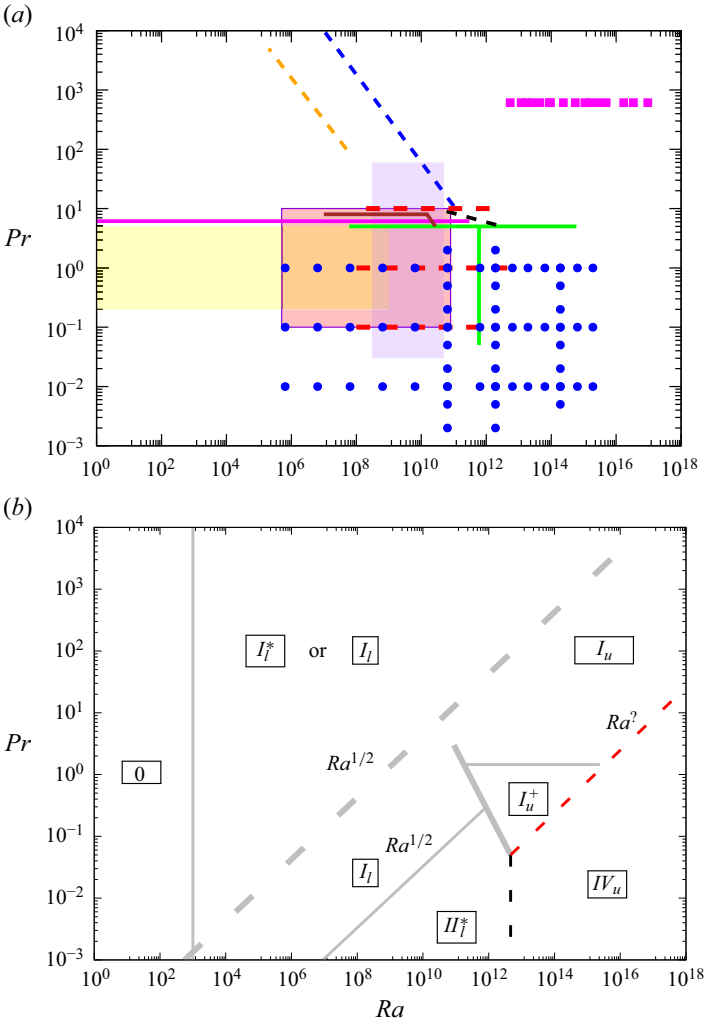

Figure 10. (*a*) Summary combining of all calculations found in the literature from experiments and DNS on HC together with the present experiments (■, magenta) and DNS from Part 1 (Passaggia & Scotti 2024) (●, blue). The plotted results also include: (- -) (blue dashed line) Rossby (1965), (- -) (orange dashed line) Miller (1968), Beardsley & Festa (1972) (—) (black dashed line), Paparella & Young (2002) (red transparent square), Siggers *et al.* (2004) (transparent yellow square), Mullarney *et al.* (2004) (black dashed line), Wang & Huang (2005) (brown line), Sheard & King (2011) (magenta horizontal line), Gayen *et al.* (2014) (green lines), Shishkina *et al.* (2017) (transparent purple square with borders) and Reiter & Shishkina (2020) (- -) (red horizontal dashed lines). (*b*) Phase diagrams in the (*Ra*, *Pr*) plane that combine the present results with Part 1 (Passaggia & Scotti 2024) at low Prandtl numbers, showing the different regimes of HC for the present flow geometry. Note that all of the above results considered no-slip boundary conditions, except for the results reported in Passaggia & Scotti (2024). In addition, dashed lines and rectangles with borders denote experiments or simulations with sidewalls.

consistent with direct numerical simulations at high *Pr* and lower *Ra*, where the effects of confinement enhance the amount of laminar dissipation and provide a mechanism for a heat transfer larger than previously theorized by Rossby (1965) for small aspect ratio domains. Increasing further the Rayleigh number beyond $Ra \gtrsim 10^{15}$ and for Prandtl numbers $Pr \approx 610$, the flow exhibits a transition back to the Rossby regime as the

boundary becomes progressively thinner. Experimental evidence of this regime is made possible following the work of Chiu-Webster *et al.* (2008), who analysed HC in the limit of asymptotically large Prandtl numbers, also known as very viscous horizontal convection. This regime is also known as the intrusion regime (Hughes & Griffiths 2008). It follows the same scaling laws as the original Rossby regime, but the structure of the flow is substantially different, with a narrow recirculating/intrusion regime while the core of the flow remains essentially at rest. Using PIV and conductivity measurements at the centre of the domain, we show that for high Rayleigh numbers, the flow follows scaling laws similar to those derived in Chiu-Webster *et al.*'s asymptotic analysis for the behaviour of the boundary layer and the thickness of the fluid at rest contained in the bulk. Definite conclusions about the magnitude of the streamfunction are harder to draw due to measurement uncertainties but hint at the same arguments.

We report a new regime transition in HC at large Rayleigh and Prandtl numbers. Combining all available evidence, we propose an updated regime diagram that extends the regime diagrams proposed by Hughes & Griffiths (2008) and more recently by Shishkina *et al.* (2016). Seven distinct regimes are mapped for which observations using either DNS or experiments have been confirmed, and the Nusselt-number dependencies are used to draw a complete regime diagram from seven orders of magnitude for the Prandtl number and seventeen orders of magnitude for the Rayleigh number. We also report the six limiting regimes known to this date and, in particular, the transition to the turbulent limiting regime IV_u for asymptotically large Rayleigh numbers and put an emphasis on the role of the aspect ratio of the domain for large Prandtl numbers. Although it was also shown that the ultimate regime IV_l cannot be achieved (Siggers *et al.* 2004; Passaggia, Scotti & White 2016; Passaggia & Scotti 2024), the present regime diagram is consistent with previous studies and reviews and provides a complete parametrization of horizontal convection that can be used for engineering and geophysical applications.

Acknowledgements. The authors thank Dr B. White, Professor D. Lohse, Dr O. Shiskina and three anonymous referees for insightful comments and encouragement.

Funding. This work was supported by the National Science Foundation (grant nos OCE–1155558 and OCE-1736989).

Declaration of interests. The authors report no conflict of interest.

Author ORCIDs.
Pierre-Yves Passaggia https://orcid.org/0000-0002-3607-7224;
Nadia F. Cohen https://orcid.org/0009-0007-3674-0990;
Alberto Scotti https://orcid.org/0000-0001-8283-3070.

References

Beardsley, R.C. & Festa, J.F. 1972 A numerical model of convection driven by a surface stress and non-uniform horizontal heating. *J. Phys. Oceanogr.* **2** (4), 444–455.

Carminati, M. & Luzzatto-Fegiz, P. 2017 Conduino: affordable and high-resolution multichannel water conductivity sensor using micro USB connectors. *Sensors Actuators* B*: Chem.* **251**, 1034–1041.

Chiu-Webster, S., Hinch, E.J. & Lister, J.R. 2008 Very viscous horizontal convection. *J. Fluid Mech.* **611**, 395–426.

Defant, A. 1961 *Physical Oceanography*, vol. 1. Pergamon.

Gayen, B., Griffiths, R.W. & Hughes, G.O. 2014 Stability transitions and turbulence in horizontal convection. *J. Fluid Mech.* **751**, 698–724.

Gayen, B., Griffiths, R.W., Hughes, G.O. & Saenz, J.A. 2013 Energetics of horizontal convection. *J. Fluid Mech.* **716**, R10.

GRAMBERG, H.J.J., HOWELL, P.D. & OCKENDON, J.R. 2007 Convection by a horizontal thermal gradient. *J. Fluid Mech.* **586**, 41–57.
GRIFFITHS, R.W. & GAYEN, B. 2015 Turbulent convection insights from small-scale thermal forcing with zero net heat flux at a horizontal boundary. *Phys. Rev. Lett.* **115** (20), 204301.
GRIFFITHS, R.W., HUGHES, G.O. & GAYEN, B. 2013 Horizontal convection dynamics: insights from transient adjustment. *J. Fluid Mech.* **726**, 559–595.
GROSSMANN, S. & LOHSE, D. 2000 Scaling in thermal convection: a unifying theory. *J. Fluid Mech.* **407**, 27–56.
HARNED, H.S. 1954 The diffusion coefficients of the alkali metal chlorides and potassium and silver nitrates in dilute aqueous solutions at 25 °C. *Proc. Natl Acad. Sci. USA* **40** (7), 551.
HUGHES, G.O. & GRIFFITHS, R.W. 2008 Horizontal convection. *Annu. Rev. Fluid Mech.* **40**, 185–208.
HUGHES, G.O., GRIFFITHS, R.W., MULLARNEY, J.C. & PETERSON, W.H. 2007 A theoretical model for horizontal convection at high Rayleigh number. *J. Fluid Mech.* **581**, 251–276.
ILICAK, M. & VALLIS, G.K. 2012 Simulations and scaling of horizontal convection. *Tellus* A **64** (1), 18377.
JEFFREYS, H. 1925 On fluid motions produced by differences of temperature and humidity. *Q. J. R. Meteorol. Soc.* **51** (216), 347–356.
KRISHNAMURTI, R. 2003 Double-diffusive transport in laboratory thermohaline staircases. *J. Fluid Mech.* **483**, 287–314.
LANDAU, L.D. & LIFSCHITZ, E.M. 1987 *Statistische Physik*. Akademie-Verlag.
LOHSE, D. & SHISHKINA, O. 2023 Ultimate turbulent thermal convection. *Phys. Today* **76** (11), 26–32.
MATUSIK, K.E. & LLEWELLYN-SMITH, S.G. 2019 The response of surface buoyancy flux-driven convection to localized mechanical forcing. *Exp. Fluids* **60** (5), 79.
MEUNIER, P. & LEWEKE, T. 2003 Analysis and treatment of errors due to high velocity gradients in particle image velocimetry. *Exp. Fluids* **35** (5), 408–421.
MILLER, R.C. 1968 A thermally convecting fluid heated non-uniformly from below. PhD thesis, Massachusetts Institute of Technology, MA.
MULLARNEY, J.C., GRIFFITHS, R.W. & HUGHES, G.O. 2004 Convection driven by differential heating at a horizontal boundary. *J. Fluid Mech.* **516**, 181–209.
PAPARELLA, F. & YOUNG, W.R. 2002 Horizontal convection is non-turbulent. *J. Fluid Mech.* **466**, 205–214.
PASSAGGIA, P.-Y., HURLEY, M.W., WHITE, B. & SCOTTI, A. 2017 Turbulent horizontal convection at high Schmidt numbers. *Phys. Rev. Fluids* **2**, 090506.
PASSAGGIA, P.-Y., LEWEKE, T. & EHRENSTEIN, U. 2012 Transverse instability and low-frequency flapping in incompressible separated boundary layer flows: an experimental study. *J. Fluid Mech.* **703**, 363–373.
PASSAGGIA, P.-Y. & SCOTTI, A. 2024 Limiting regimes of turbulent horizontal convection. Part 1. intermediate and low Prandtl numbers. *J. Fluid Mech.* **997**, A5.
PASSAGGIA, P.-Y., SCOTTI, A. & WHITE, B. 2016 Global stability and flow transition in horizontal convection. *International Symposium on Stratified Flows* **8**, https://escholarship.org/uc/item/49956025.
RAMME, L. & HANSEN, U. 2019 Transition to time-dependent flow in highly viscous horizontal convection. *Phys. Rev. Fluids* **4** (9), 093501.
REITER, P. & SHISHKINA, O. 2020 Classical and symmetrical horizontal convection: detaching plumes and oscillations. *J. Fluid Mech.* **892**, R1.
ROCHA, C., CONSTANTINOU, N.C., SMITH, S.G.L. & YOUNG, W.R. 2020 The Nusselt number of horizontal convection, *J. Fluid Mech*. **894**, A24.
ROSEVEAR, M.G., GAYEN, B. & GRIFFITHS, R.W. 2017 Turbulent horizontal convection under spatially periodic forcing: a regime governed by interior inertia. *J. Fluid Mech.* **831**, 491–523.
ROSSBY, H.T. 1965 On thermal convection driven by non-uniform heating from below: an experimental study. *Deep-Sea Res.* **12**, 9–16.
ROSSBY, T. 1998 Numerical experiments with a fluid heated non-uniformly from below. *Tellus* A **50**, 242–257.
SANDSTRÖM, J.W. 1908 Dynamische versuche mit meerwasser. *Ann. Hydrogr. Marit. Meteorol.* **36**, 6–23.
SANDSTRÖM, J.W. 1916 Meteorologische Studien im schwedischen Hochgebirge. *Göteborgs Kungl. Vet. Handl.* **17** (4), 48.
SHEARD, G.J. & KING, M.P. 2011 Horizontal convection: effect of aspect ratio on Rayleigh number scaling and stability. *Appl. Math. Model.* **35** (4), 1647–1655.
SHISHKINA, O., EMRAN, M.S., GROSSMANN, S. & LOHSE, D. 2017 Scaling relations in large-Prandtl-number natural thermal convection. *Phys. Rev. Fluids* **2** (10), 103502.
SHISHKINA, O., GROSSMANN, S. & LOHSE, D. 2016 Heat and momentum transport scalings in horizontal convection. *Geophys. Res. Lett.* **43** (3), 1219–1225.
SHISHKINA, O. & WAGNER, S. 2016 Prandtl-number dependence of heat transport in laminar horizontal convection. *Phys. Rev. Lett.* **116** (2), 024302.

SIGGERS, J.H., KERSWELL, R.R. & BALMFORTH, N.J. 2004 Bounds on horizontal convection. *J. Fluid Mech.* **517**, 55–70.

STEWART, K.D., HUGHES, G.O. & GRIFFITHS, R.W. 2012 The role of turbulent mixing in an overturning circulation maintained by surface buoyancy forcing. *J. Phys. Oceanogr.* **42** (11), 1907–1922.

SVERDRUP, H.U., JOHNSON, M.W. & FLEMING, R.H. 1942 *The Oceans: Their Physics, Chemistry, and General Biology*, vol. 7. Prentice-Hall.

WANG, W. & HUANG, R.X. 2005 An experimental study on thermal circulation driven by horizontal differential heating. *J. Fluid Mech.* **540**, 49–73.

WHITEHEAD, J.A. & WANG, W. 2008 A laboratory model of vertical ocean circulation driven by mixing. *J. Phys. Oceanogr.* **38** (5), 1091–1106.